

Time dependent quantum transport through Kondo correlated quantum dots

A. Goker¹ and E. Gedik²

¹ *Department of Physics,
Bilecik University,
11210, Gölümbe, Bilecik, Turkey and*

² *Department of Physics,
Eskisehir Osmangazi University,
26480, Meselik, Eskisehir, Turkey*

(Dated: July 25, 2018)

In this chapter, we review recent work about time dependent quantum transport through a quantum dot in Kondo regime. This represents a major step towards designing next generation transistors that are expected to replace current MOSFET's in a few years. We first discuss the effects of the density of states of gold contacts on the instantaneous conductance of an asymmetrically coupled quantum dot that is abruptly moved into Kondo regime via a gate voltage. Next, we investigate the effect of strong electron-phonon coupling on the dot on the instantaneous conductance. Finally, we discuss thermoelectric effects using linear response Onsager relations for a quantum dot that is either abruptly moved into Kondo regime or driven sinusoidally via a gate voltage. We explain encountered peculiarities in transport based on the behaviour of the density of states of the dot and the evolution of the Kondo resonance.

PACS numbers: 72.15.Qm, 85.35.-p, 71.15.Mb

I. INTRODUCTION

Single electron transistors are nanodevices made up of a discrete energy level sandwiched between electrodes. They are expected to have profound implications in designing next generation transistors since conventional MOSFET's will reach their physical limit at 10 nm in a few years¹. The rapid evolution of this field derived extra benefit from unprecedented control over nanodevices brought forward by nanotechnology revolution. It is imperative that the switching behaviour of these next generation transistors are examined carefully before they are integrated into electrical circuits. Furthermore, the field of time dependent quantum transport through nanostructures should also help calibrate quantum computers² and single electron guns³.

Several time scales emerged^{4,5} after the initial studies about the effect of a strongly correlated state called Kondo effect on the transient current ensuing after a sudden shift of the gate or bias voltage⁶⁻⁸. In section II of this chapter, we will investigate the damped oscillations in the long timescale for an asymmetrically coupled system⁹⁻¹¹ arising as a result of strong interference between the Kondo resonance and the Van Hove singularities in the contacts' density of states.

In section III, we will consider the effect of strong electron-phonon coupling on the instantaneous current through a single electron transistor abruptly moved into Kondo regime via a gate voltage. We will find out that the instantaneous current exhibits damped sinusoidal oscillations in the long timescale even in infinitesimal bias¹². We will elaborate on the origin of this phenomena based on the behaviour of the density of states of the dot.

Thermopower (Seebeck coefficient) can provide clue

about the alignment of the dot level with respect to the Fermi level of the contacts hence it is a valuable tool to determine the existence of Kondo resonance. This has been verified with several recent experiments as well¹³⁻¹⁶.

Different groups pointed out that the sign of thermopower in Kondo regime depends quite sensitively on position of the dot level^{17,18}. In section IV, we will summarize recent efforts to study the transient behaviour of thermopower. We will start by discussing the behaviour of thermopower when the the dot energy level is suddenly shifted to a position near the Fermi level¹⁹. We will show that the inverse of the saturated decay time of thermopower to its steady state value is equal to the Kondo temperature.

Time dependent ac perturbations of the dot energy level allows monitoring instantaneous thermopower when the Kondo temperature changes constantly due to the sinusoidal motion of the dot level^{20,21}. Experimental developments on adjusting dot-lead coupling enabled this so called Kondo shuttling^{22,23}. Previously, it was found that the time averaged conductance deviates significantly from its monotonic decrease as a function of applied bias when the bias is equal to the driving frequency of the dot level²⁴. In the latter part of section IV, we will investigate in detail the instantaneous and time averaged values of the thermopower when the dot level is driven sinusoidally by means of a gate voltage²⁵.

Before we move on to discuss the results, we would like to outline the theoretical framework for our calculations. We will model the single electron transistor with a single discrete degenerate energy level ε_{dot} coupled to the electrodes. Anderson Hamiltonian sufficiently describes the

physics of this set-up. It is given by

$$H(t) = \sum_{\sigma} \varepsilon_{dot}(t) n_{\sigma} + \sum_{k\alpha\sigma} \varepsilon_k n_{k\alpha\sigma} + \frac{1}{2} \sum_{\sigma,\sigma'} U_{\sigma,\sigma'} n_{\sigma} n_{\sigma'} + \sum_{k\alpha\sigma} \left[V_{\alpha}(\varepsilon_{k\alpha}, t) c_{k\alpha\sigma}^{\dagger} c_{\sigma} + \text{H.c.} \right], \quad (1)$$

where c_{σ}^{\dagger} (c_{σ}) and $c_{k\alpha\sigma}^{\dagger}$ ($c_{k\alpha\sigma}$) with $\alpha=L,R$ create (annihilate) an electron of spin σ in the dot energy level and in the left(L) and right(R) electrodes respectively. The n_{σ} and $n_{k\alpha\sigma}$ are the number operators for the dot level and the electrode α . V_{α} are the tunneling amplitudes between the electrode α and the quantum dot. The Coulomb repulsion U is taken to be infinite. This choice restricts the occupation of the dot level to unity. In this chapter, we will adopt atomic units where $\hbar = k_B = e = 1$.

In our method, slave boson transformation is carried out for the Anderson Hamiltonian. In this procedure, ordinary electron operators on the dot are expressed in terms of a massless (slave) boson operator and a pseudofermion operator as

$$c_{\sigma} = b^{\dagger} f_{\sigma}, \quad (2)$$

subject to

$$Q = b^{\dagger} b + \sum_{\sigma} f_{\sigma}^{\dagger} f_{\sigma} = 1. \quad (3)$$

This last requirement is needed to prevent the double occupancy in the original Hamiltonian when $U \rightarrow \infty$. This transformation enables drop the quartic Hubbard term while retaining its effects in other terms. The transformed Hamiltonian turns out to be

$$H(t) = \sum_{\sigma} \varepsilon_{dot}(t) n_{\sigma} + \sum_{k\alpha\sigma} \left[\varepsilon_k n_{k\alpha\sigma} + V_{\alpha}(\varepsilon_{k\alpha}, t) c_{k\alpha\sigma}^{\dagger} b^{\dagger} f_{\sigma} + \text{H.c.} \right], \quad (4)$$

where f_{σ}^{\dagger} (f_{σ}) and b^{dag} (b) with $\alpha=L,R$ create(annihilate) an electron of spin σ and a slave boson on the dot respectively.

Hopping matrix elements will be assumed to have no explicit time dependency. Consequently, the coupling of the quantum dot to the electrodes can be expressed as $\Gamma_{L(R)}(\epsilon) = \bar{\Gamma}_{L(R)} \rho_{L(R)}(\epsilon)$, where $\bar{\Gamma}_{L(R)}$ is a constant given by $\bar{\Gamma}_{L(R)} = 2\pi |V_{L(R)}(\epsilon_f)|^2$ and $\rho_{L(R)}(\epsilon)$ is the density of states function.

The retarded Green function can then be redefined in terms of the slave boson and pseudofermion Green functions⁹ as

$$G^R(t, t_1) = -i\theta(t - t_1) [G_{pseudo}^R(t, t_1) B^<(t_1, t) + G_{pseudo}^<(t, t_1) B^R(t_1, t)]. \quad (5)$$

It is a quite a cumbersome and highly nontrivial task to compute the values of these double time Green functions

in real time. This is managed by solving coupled integro-differential Dyson equations in a two-dimensional cartesian grid. The self-energies of the pseudofermion and slave boson are key ingredients into these equations. We utilize quite versatile non-crossing approximation(NCA) for this purpose^{5,26}. NCA discards higher order corrections in which propagators cross each other. Therefore, it has certain drawbacks such as giving unphysical results in finite magnetic fields and when the ambient temperature is an order of magnitude smaller than Kondo energy scale. These regimes will be avoided in this chapter. Main advantage of NCA is that it is a quite powerful technique to obtain accurate results for dynamical quantities. Once the Dyson equations are solved, their values are stored in a square matrix which is propagated in discrete steps in time in diagonal direction.

Kondo effect is considered a prime example of many body physics occurring at low temperatures as a result of the coupling between the net spin localized within the dot and the continuum electrons of a metal in its vicinity. Its main revelation is a sharp resonance formed around the Fermi level of the metal. The linewidth of this Kondo resonance is on the order of a low energy scale called the Kondo temperature which is denoted by T_K and expressed as

$$T_K \approx \left(\frac{D\Gamma_{tot}}{4} \right)^{\frac{1}{2}} \exp \left(-\frac{\pi |\epsilon_{dot}|}{\Gamma_{tot}} \right), \quad (6)$$

In Eq. (6) D is the half bandwidth of the conduction electrons of the electrode whereas $\Gamma_{tot} = (\bar{\Gamma}_L + \bar{\Gamma}_R)\rho(\epsilon_f)$.

II. DESIGNER SWITCHES

In this section, we will study the instantaneous conductance for a situation where the dot level is abruptly shifted from $\epsilon_1 = -5\Gamma_{tot}$ to $\epsilon_2 = -2\Gamma_{tot}$ where $\Gamma_{tot} = 0.8$ eV at $t = 0$ by a gate voltage. Both contacts were assumed to be made up of gold whose density of states is shown in Fig. 1. The density of states of the gold contacts were obtained with the ab initio calculations which invoked the full-potential linearized augmented plane wave (FP-LAPW) method using WIEN2K package²⁷. The generalized gradient approximation devised by Perdew, Burke, and Ernzerhof (GGA-PBE) form²⁸ was utilized as exchange-correlation functional in all ab initio calculations. The core states of gold atom were taken to be in an electronic configuration of (Kr, $4d^{10}4f^{14}5s^2$). The valence states include $5p$, $5d$, $6s$, and $6p$. Our calculations invoked the unit cell of *fcc* Au (space group $Fm\bar{3}m$, $a = 4.080$ Å) with 4 atoms per cell.

We carried out a fitting procedure using six different Gaussians with various linewidth and peak positions to mimic the density of states of gold. This enabled us to express the density of states of gold in a functional form. The resulting best fit curves are also shown in red in Fig. 1.

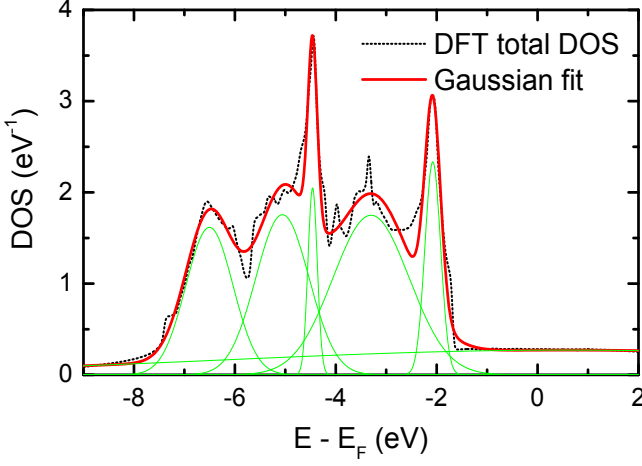


FIG. 1: Density of states of gold calculated using DFT is shown with black dashed curve as a function of separation from the Fermi level. Red curve corresponds to the best fit to the ab initio data by using a linear combination of Gaussian functions. Each individual Gaussian function is also shown with green curves.

The net current is obtained from the pseudofermion and slave boson Green's functions $G_{pseu}^{<(R)}(t, t')$ and $B^{<(R)}(t, t')$. The general expression for the net current²⁹ can be rewritten by using these Green's functions⁹. The final expression is given by

$$I(t) = -2(\bar{\Gamma}_L - \bar{\Gamma}_R) \text{Re} \left(\int_{-\infty}^t dt_1 \xi_o(t, t_1) h(t - t_1) \right) + 2\bar{\Gamma}_L \text{Re} \left(\int_{-\infty}^t dt_1 (\xi_o(t, t_1) + \xi_u(t, t_1)) f_L(t - t_1) \right) - 2\bar{\Gamma}_R \text{Re} \left(\int_{-\infty}^t dt_1 (\xi_o(t, t_1) + \xi_u(t, t_1)) f_R(t - t_1) \right) \quad (7)$$

with $\xi_o(t, t_1) = G_{pseu}^{<}(t, t_1) B^R(t_1, t)$ and $\xi_u(t, t_1) = G_{pseu}^R(t, t_1) B^{<}(t_1, t)$. In Eq. (7), $f_L(t - t_1)$ and $f_R(t - t_1)$ are the convolution of the density of states function with the Fermi-Dirac distributions of the left and right contacts respectively, whereas $h(t - t_1)$ is the Fourier transform of the DOS⁹. The conductance G is equal to the current divided by the bias voltage V . $\eta = \frac{\bar{\Gamma}_L}{\bar{\Gamma}_{tot}}$, where $\bar{\Gamma}_{tot} = \bar{\Gamma}_L + \bar{\Gamma}_R$, will be called the asymmetry factor.

We assume that the dot level is switched to its final position at $t=0$. In the initial short timescale corresponding to $\Gamma t \leq 5$, the conductance attains a maximum value for large asymmetry factors before starting to decay in agreement with previous studies⁹. The instantaneous conductance in the long Kondo timescale is shown in Fig. 2. It is clear that a complex ringing is taking place here and the amplitude of the oscillations dwindles as the asymmetry factor is reduced. Oscillations completely die out for symmetric coupling since the interference between the left contact and the Kondo resonance is out of phase with

the interference between the right contact and the Kondo resonance due to opposite signs in Eq. (7). The amplitudes of two simultaneous interference effects are equal for symmetric coupling hence the oscillations cancel each other.

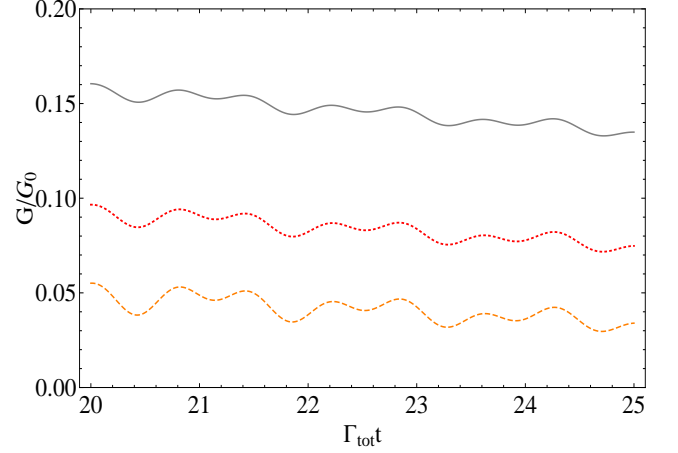


FIG. 2: Grey, red and orange curves from top to bottom show the instantaneous conductance versus time in Kondo timescale after the dot level has been switched to its final position for asymmetry factors of 0.95, 0.9 and 0.85 respectively at $T=0.009\Gamma_{tot}$ and $V=T_K$ for constant Γ_{tot} .

Fourier transform of the time dependent conductance reveals all the frequency components causing the complex fluctuation pattern. This analysis provides two distinct frequencies, ω_1 and ω_2 , which give rise to beating with envelope and carrier frequencies of $\omega_1 - \omega_2$ and $\omega_1 + \omega_2$, respectively. It turns out that $\omega_1 = 2.15\omega_2$ corresponding to the ratio of the separation of the peaks at -2.08 eV and -4.46 eV in Fig. 1 from the Fermi level. This outcome is a clear evidence that the transient current in the Kondo regime is a tool to detect the discontinuities in the density of states of the electrodes.

The influence of finite bias is displayed in Fig. 3. Finite bias quenches the amplitude of oscillations. Moreover, the decay rate of these oscillations, defined to be the inverse of the time required for them to disappear, increases. This is a clue about the relation of these oscillations to the formation of the Kondo resonance.

Fig. 4 demonstrates the effect of ambient temperature. The decay rate of the oscillations decreases upon reducing the ambient temperature. Furthermore, lower ambient temperatures increases the amplitude of the oscillations. However, it saturates when the temperature approaches the Kondo temperature T_K . Lowering the temperature below T_K doesn't change the amplitude.

We now would like to analyze the effect of specific contact geometry on transient current. To this end, we studied three geometries, i.e. (001)-surface, (111)-surface and (111)-pyramid to simulate the Au electrode profile as shown in Fig. 5. Atomic slabs with 13 Au layers have been used to build these three geometries. The distance between the two opposite electrodes is 30 Bohr radius

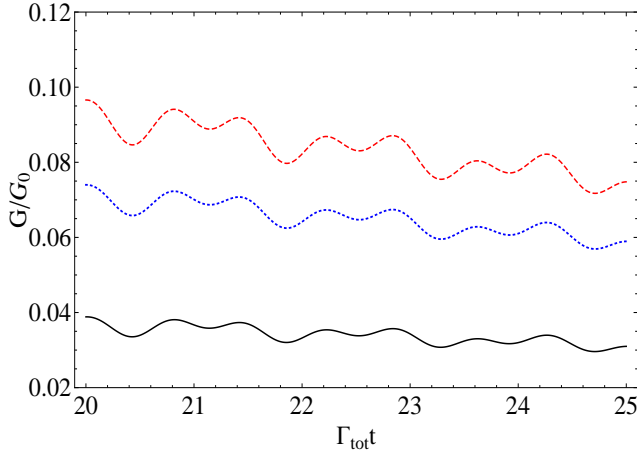


FIG. 3: Red, blue and black curves from top to bottom represent the instantaneous conductance versus time in Kondo timescale after the dot level has been switched to its final position for asymmetry factor of 0.9 at $T=0.009\Gamma_{tot}$ when the bias is equal to $V=T_K$, $V=4T_K$ and $V=8T_K$ respectively for constant Γ_{tot} .

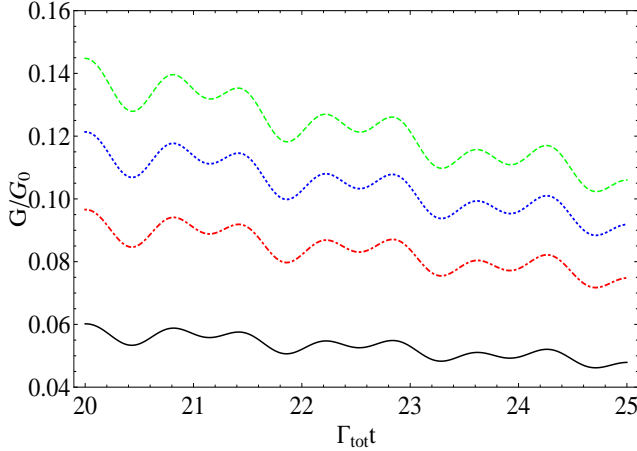


FIG. 4: Green, black, blue, red and purple curves from top to bottom show the instantaneous conductance versus time in Kondo timescale after the dot level has been switched to its final position for asymmetry factor of 0.9 at $T=0.0015\Gamma_{tot}$, $T=0.0060\Gamma_{tot}$, $T=0.0090\Gamma_{tot}$ and $T=0.0150\Gamma_{tot}$ respectively for constant Γ_{tot} with a bias of $V=T_K$.

in all cases. The exchange-correlation potential of the generalized gradient approximation within the Perdew, Burke, and Ernzerhof (GGA-PBE) form²⁸ has been used in all calculations. The plane wave cut-off has been determined by $R_{mt}K_{max} = 6.5$ and $l_{max} = 10$. K-mesh of $30 \times 30 \times 3$, $36 \times 36 \times 2$ and $6 \times 6 \times 2$ have been adopted for (001)-surface, (111)-surface and (111)-pyramid respectively. Note that only the DOS of topmost atoms, which are relevant to the transport properties between electrodes in the surface/pyramid structures, will be used in the following many body calculations. The resulting density of states is shown in Fig. 6.

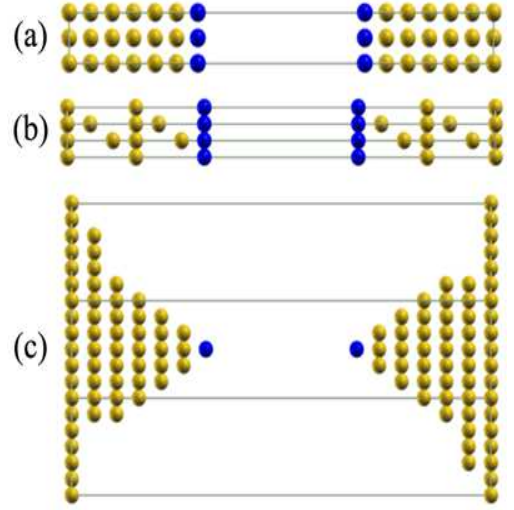


FIG. 5: This figure shows the three geometries, (a) (001)-surface, (b) (111)-surface and (c) (111)-pyramid, used to simulate the profile of Au electrode. The Au atoms in blue color are the atoms relevant to the transport properties between electrodes in all three structures.

We will be concerned with the transient current ensuing after the dot level is switched from $\epsilon_1 = -4\Gamma_{tot}$ to $\epsilon_2 = -2\Gamma_{tot}$ at $t=0$ via a gate voltage. For all three geometries, this triggers an abrupt shift from a non-Kondo state to a Kondo state. It is worth mentioning that the Kondo temperature in the final state is slightly lower for (111) pyramid than the other two geometries due to the shorter conduction electron bandwidth in Fig. 1.

Time dependent conductance results are displayed in Fig. 7 for all three geometries in infinitesimal bias. Short timescale is omitted here due to the resemblance to previous studies⁹. The most striking feature in this figure is the extreme variations in conductance fluctuations among the three geometries. This effect can only originate from the difference in band structure of the contacts because all other parameters are kept fixed. We should point out that the slight difference between the Kondo temperature of (111) pyramid and the other two geometries does not change the relative behaviour of the fluctuations for these geometries because T/T_K scaling has been shown to alter only the amplitude of the fluctuations⁹. Consequently, the overall pattern is unaffected.

These fluctuations are obviously the result of an admixture of sinusoidal oscillations with different frequencies and amplitudes. Fourier transform of the instantaneous conductance gives each frequency component. It turns out that the frequencies are proportional to the separation between the peak positions and the Fermi level for all cases. This is precisely why instantaneous current for (001) surface exhibits a more erratic pattern compared to the others as five distinct frequencies contribute to it. Moreover, there are other peaks that appear in ac-

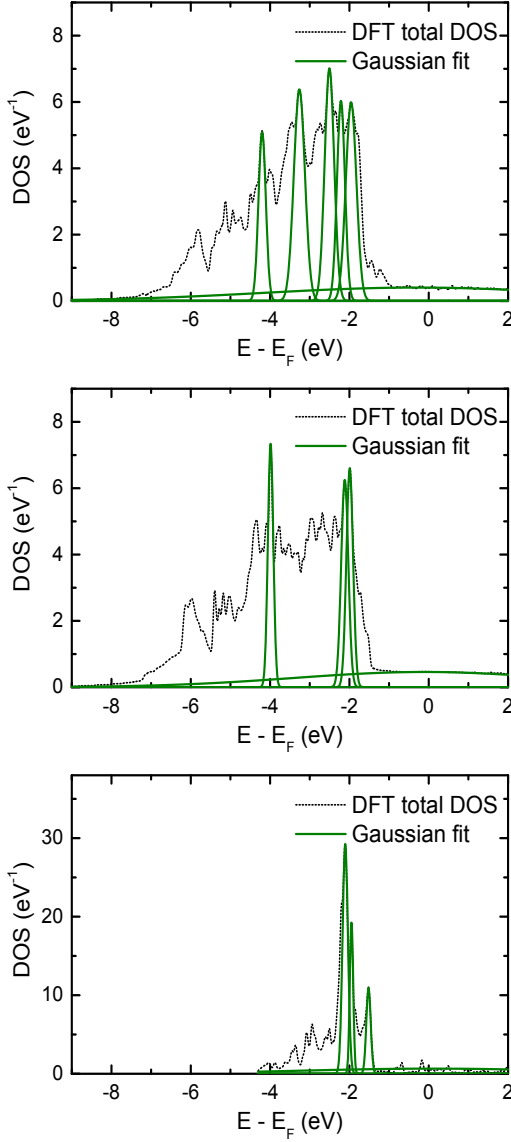


FIG. 6: Density of states of (001) surface, (111) surface and (111) pyramid calculated using DFT is shown with black dashed curve from top to bottom respectively as a function of separation from the Fermi level. Each Gaussian used to capture the sharp features and the Fermi level is also shown with green curves in each geometry.

tual DFT data but they were excluded from our fitting since they have negligible contribution to the fluctuation pattern. The oscillation amplitude associated with them is quite small to cause a noticeable effect because they are either located far away from the Fermi level or the peaks are not prominent compared to the surrounding features.

A microscopic mechanism for these instantaneous conductance results can be inferred with the aid of the evolution of the dot density of states. Based on the fact that discontinuities in the density of states of the contacts can interfere with the Kondo resonance when $\eta \neq 1^9$, we

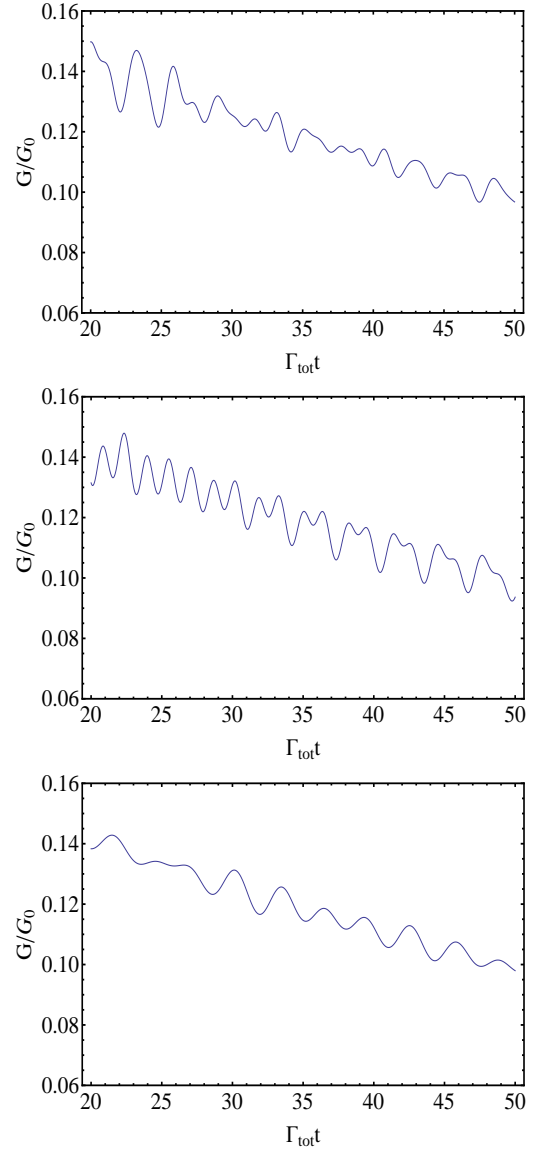


FIG. 7: Panels from top to bottom show the instantaneous conductance versus time in Kondo timescale after the dot level has been switched to its final position for (001) surface, (111) surface and (111) pyramid respectively with an asymmetry factor of 0.9 at $T=0.009\Gamma_{tot}$ in infinitesimal bias.

propose that the fluctuations in time dependent conductance stem from the interference between the emerging Kondo resonance at the Fermi level and the sharp features in the density of states. Despite the static nature of the sharp features, the Kondo resonance evolves in time in a dynamical way. Consequently, the fluctuations continue until the Kondo resonance is fully formed. Furthermore, the reduction of oscillation amplitudes with increasing source-drain bias is related to the destruction of the Kondo resonance which diminishes the interference. This scenario is also supported by the saturation of oscillation amplitudes below the Kondo temperature because

the Kondo resonance is fully developed below this energy scale. Consequently, the interference strength does not change upon lowering the ambient temperature any further.

III. VIBRATING SET

In this section, we will present results about a quantum dot which experiences strong electron-phonon interaction. In our approach, electron-phonon coupling term is eliminated from the Holstein Hamiltonian via Lang-Firsov canonical transformation. This results in renormalized dot energy level and Hubbard interaction strength. We then perform slave boson transformation and invoke the non-crossing approximation to solve the resulting Dyson equations. The technical details of this implementation can be found elsewhere¹².

We will again consider the ramifications of the sudden motion of the dot level from a position well below the Fermi level to a position where the Kondo effect is present with a gate voltage. Previous studies proved that the Kondo resonance which is pinned to the Fermi level of the contacts acquires sidebands on each side due to the electron-phonon coupling. Nevertheless, the transient dynamics of this system as a response to abrupt perturbations is unexplored. Fig. 8 depicts the system schematically.

The instantaneous conductance results immediately after the dot level has been switched to its final position are shown in Fig. 9. These data have been taken for three different temperatures for a constant nonzero electron-phonon coupling g , which is defined as the square of the ratio of electron-phonon coupling strength λ to phonon frequency ω . Instantaneous conductance results for $g=0$ has been known for sometime⁴. The Kondo timescale where the development of the Kondo resonance takes place occurs between $10 < \Gamma t < 60$ in Fig. 9.

The steady state conductances (i.e. $\Gamma t \rightarrow \infty$) are smaller than the case for $g=0$ in Fig. 9 for all temperatures. This is simply because the electron-phonon coupling gradually suppresses the Kondo resonance³⁰. This suppression has been attributed to the downward shift of the energy level due to the phonon reorganization. This originates from the renormalization of the dot level.

Another subtlety is the sinusoidal oscillations of the instantaneous conductance in the Kondo timescale. These oscillations cannot be discerned in the main panel of Fig. 9. Main panel is magnified in the inset of Fig. 9 where conductance curves are shifted in such a way that they overlap at the onset of oscillations. It is obvious from here that the oscillation frequency is the same for all temperatures. Furthermore, the amplitude of the oscillations decreases with increasing ambient temperature and the oscillation frequency happens to be equal to the phonon frequency ω_0 .

We then performed the previous calculation at same ambient temperatures for a higher g value to check

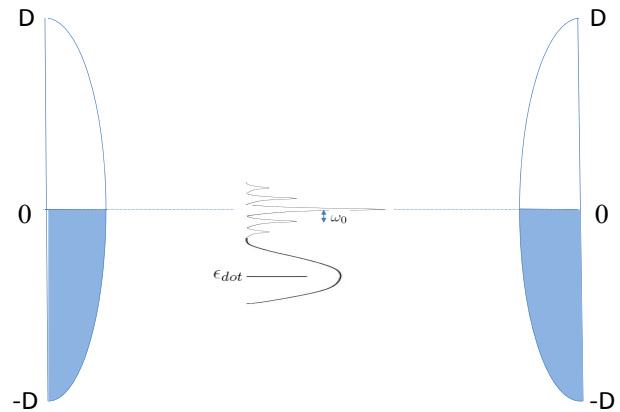


FIG. 8: This figure illustrates the density of states of both contacts alongside with the application of an ac gate voltage to the dot energy level as well as the temperature gradient between the contacts.

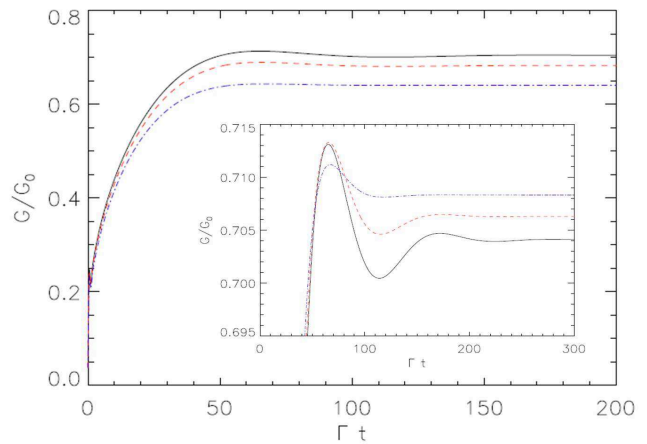


FIG. 9: This figure illustrates the density of states of both contacts alongside with the application of an ac gate voltage to the dot energy level as well as the temperature gradient between the contacts.

whether oscillation frequency changes. Fig. 10 depicts the outcome. Increasing g lowers the steady state conductance for all temperatures as anticipated because the the dot level is shifted down due to renormalization. More interestingly, frequency of the conductance oscillations is unchanged and again equal to the phonon frequency ω_0 . This is a quite remarkable and arresting result. We want to point out that we changed g in our calculations by increasing λ and keeping ω_0 constant to enable a direct comparison. Further calculations with other g values proved that the oscillation frequency stays at ω_0 for all g values.

The instantaneous conductance exhibits oscillations in the short timescale (i.e. $0 < \Gamma t < 10$) related to the charge transfer^{4,31} as well. These oscillations are shown in the inset of Fig. 10. These oscillations are not related

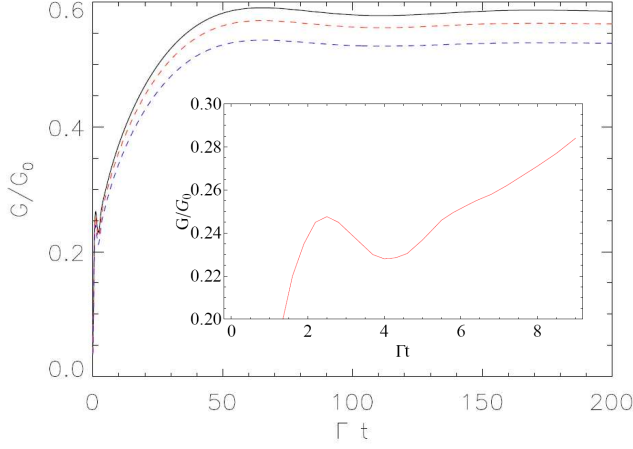


FIG. 10: This figure illustrates the density of states of both contacts alongside with the application of an ac gate voltage to the dot energy level as well as the temperature gradient between the contacts.

to the formation of the Kondo resonance because spin-flip processes are yet to begin here. The frequency of these oscillations have been found to be proportional to the final dot level⁴.

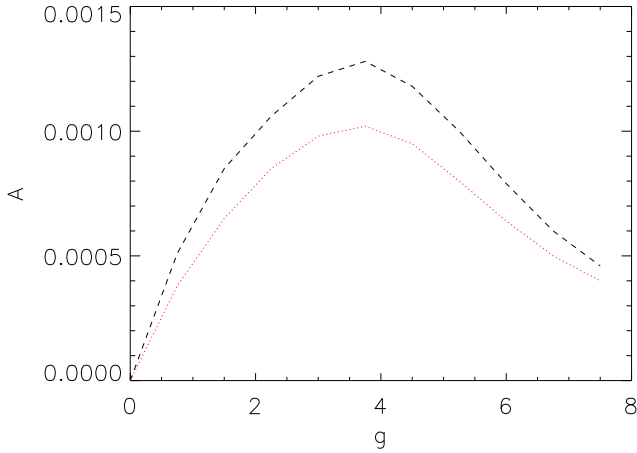


FIG. 11: This figure illustrates the density of states of both contacts alongside with the application of an ac gate voltage to the dot energy level as well as the temperature gradient between the contacts.

Fig. 11 displays the behaviour of the amplitude of oscillations as a function of g at two different temperatures. The amplitude is zero at $g=0$ for both cases but it starts to increase gradually until it reaches a peak before $g=4$. It then starts decreasing and approaches zero for large g values. Furthermore, we see that lowering temperature results in larger oscillation amplitudes for all g values. Our calculations at other temperatures showed that this conclusion is general and valid for other ambient temperatures too.

We propose the interference between the main Kondo resonance and its phonon sidebands as the underlying microscopic mechanism for the sinusoidal oscillations seen in the instantaneous conductance in the Kondo timescale. Previous investigations demonstrated clearly that the phonon sidebands are separated from the main Kondo peak by an integer multiple of phonon frequency ω_0 ^{32–35}. That is why the frequency of oscillations always turns out to be equal to ω_0 . For a given g , the amplitude of oscillations increases with decreasing ambient temperature because both the main Kondo peak and its phonon satellites are more robust. Consequently, interference between them is stronger. When $g=0$, the amplitude of oscillations is zero because phonon sidebands do not exist in this limit. Even though the main Kondo peak is quenched somewhat for small g , its phonon sidebands become slightly more pronounced³⁶, thus the amplitude of oscillations starts to grow. Nevertheless, the amplitudes start decreasing around $g=4$ since all peaks start to get inhibited. The amplitude vanishes for large g where the Kondo effect is destroyed completely and all peaks are gone.

IV. THERMOELECTRIC EFFECTS

In this chapter, we will be interested in Seebeck coefficient or thermopower of this device. In linear response, it is given by

$$S(t) = \frac{L_{12}(t)}{T L_{11}(t)}, \quad (8)$$

where the Onsager coefficients are

$$L_{11}(t) = T \times \text{Im} \left(\int_{-\infty}^t dt_1 \int \frac{d\epsilon}{2\pi} e^{i\epsilon(t-t_1)} \Gamma(\epsilon) G^r(t, t_1) \frac{\partial f(\epsilon)}{\partial \epsilon} \right) \quad (9)$$

and

$$L_{12}(t) = T^2 \times \text{Im} \left(\int_{-\infty}^t dt_1 \int \frac{d\epsilon}{2\pi} e^{i\epsilon(t-t_1)} \Gamma(\epsilon) G^r(t, t_1) \frac{\partial f(\epsilon)}{\partial T} \right) \quad (10)$$

We will first study the behaviour of the instantaneous thermopower immediately after the dot level is switched from $\epsilon_1 = -5\Gamma$ to $\epsilon_2 = -2\Gamma$ at $t=0$ via a gate voltage for a symmetrically coupled system. Kondo resonance starts to emerge in the final state as a result of this transition. Fig.12 shows the density of states of the dot both in initial and final levels plus the density of states of the contacts schematically.

Fig. 13 shows instantaneous thermopower at various ambient temperatures immediately after the dot level was switched to its final position in infinitesimal bias for $g=0$. It is clear that the transient thermopower decays from zero to its steady state value for all temperatures and this

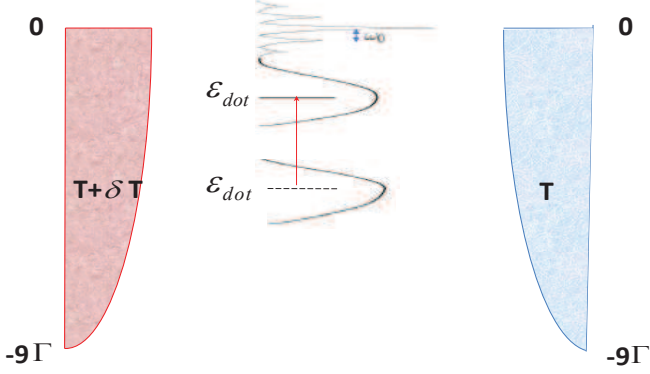


FIG. 12: This figure shows the density of states of both contacts and the quantum dot in the initial and final states schematically. The temperature gradient between the contacts is also depicted.

steady state value is always negative. On the other hand, the absolute value of steady state thermopower goes up with decreasing temperature until it reaches a maximum at a critical temperature. It starts to decrease if the temperature is lowered any further. However, the decay time, defined as the time required to reach the steady state value, remains constant. This critical temperature has been shown to be equal to the Kondo temperature¹⁸. Saturation of the decay time of thermopower below Kondo temperature is the new physics our results reveal.

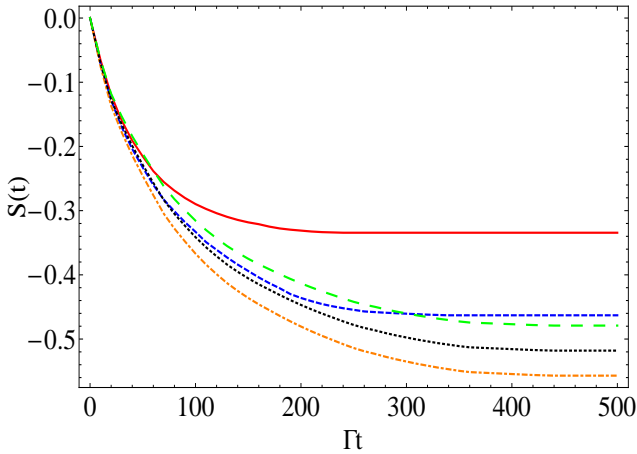


FIG. 13: This figure shows the instantaneous thermopower $S(t)$ immediately after the dot level has been moved to its final position for $T_1=0.0035\Gamma$ (red solid), $T_2=0.0028\Gamma$ (blue short dashed), $T_3=0.0021\Gamma$ (orange dot dashed), $T_4=0.0014\Gamma$ (black dotted), $T_5=0.0007\Gamma$ (green long dashed) in linear response without any electron-phonon coupling.

Fig. 14 displays the instantaneous thermopower for the same parameters used in Fig. 13. The difference is that

we turn on electron-phonon interaction and take $g=2.25$ with $\omega_0=0.08\Gamma$. In this case, the dot level is shifted slightly downwards due to renormalization leading to a smaller Kondo temperature. Smaller Kondo temperature due to the renormalization of the dot level cause steady state thermopower to be less than $g=0$ case provided that the ambient temperature is above both Kondo temperatures. However, steady state thermopower exceeds the value attained at $g=0$ case when the ambient temperature falls below both Kondo temperatures.

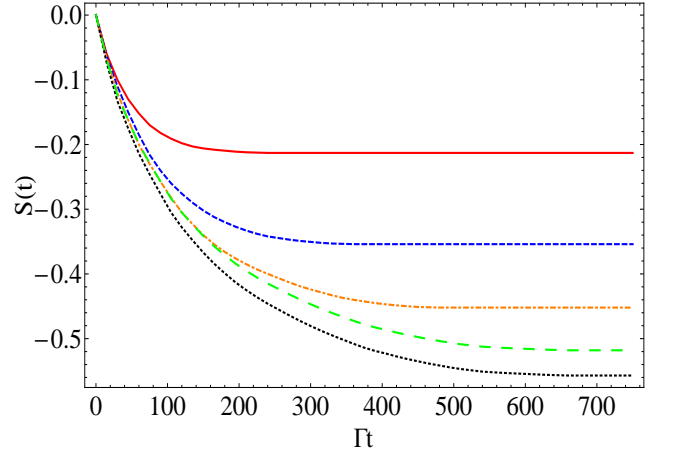


FIG. 14: This figure shows the instantaneous thermopower $S(t)$ immediately after the dot level has been moved to its final position for $T_1=0.0035\Gamma$ (red solid), $T_2=0.0028\Gamma$ (blue short dashed), $T_3=0.0021\Gamma$ (orange dot dashed), $T_4=0.0014\Gamma$ (black dotted), $T_5=0.0007\Gamma$ (green long dashed) in linear response for $g=2.25$.

The major difference with $g=0$ case is the duration of the saturated decay time. It is now much longer as lowest curves in both Fig. 13 and Fig. 14 clearly show. The decay time of thermopower scales with $1/T_K$ according to our calculations. This scaling is reminiscent to previous time dependent conductance calculations⁴. The fundamental mechanism is the same for both situations because they rely on the evolution of Kondo resonance whose development is inversely proportional to the Kondo temperature⁶.

We want to provide a microscopic explanation for the numerical results presented above. The relation between the dot density of states and the thermopower at low temperatures is given by the Sommerfeld expansion. It can be cast as

$$S(T) = -\frac{\pi^2 T}{3A(0, T)} \frac{\partial A}{\partial \epsilon} \Big|_{\epsilon=0} \quad (11)$$

in atomic units. Here, $A(0, T)$ is the value of the dot density of states at Fermi level and $\frac{\partial A}{\partial \epsilon}$ is its derivative. The Kondo resonance is formed slightly above the Fermi level³⁷ causing the derivative of the dot density of states at Fermi level to be positive. This will naturally generate a negative thermopower in Kondo regime. Otherwise,

the thermopower will be positive without the Kondo resonance because the only prominent feature of the dot density of states is the Breit-Wigner resonance in that case.

The Kondo resonance is in its most developed form when $T \leq T_K$. Therefore, the decay time of thermopower stays constant below T_K . On the other hand, the steady state value keeps decreasing due to the T prefactor at the beginning of Sommerfeld expansion which is the only variable below T_K . Furthermore, $S(t)=0$ at $t=0$ because the Kondo resonance does not exist when the dot is in its initial level since $T \gg T_K$. This means that the dot density of states is essentially flat at Fermi level. This in turn implies zero slope resulting in zero thermopower.

Finally, we want to investigate the behaviour of Eq. (8) for a quantum dot in Kondo regime whose energy level is displaced sinusoidally via a gate voltage. Time averaged thermopower has been previously investigated for this set-up without the Kondo resonance³⁸. It is quite intriguing to add strong correlation effects to this model since they play a significant role in confined nanostructures like quantum dots. We will again be restricted to the linear response thermopower because the Onsager relations are valid only in this regime.

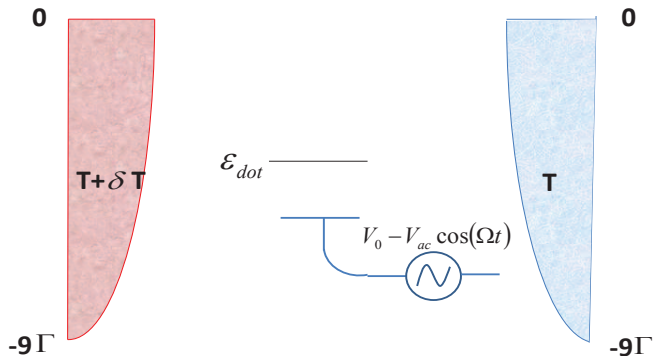


FIG. 15: This figure illustrates the density of states of both contacts alongside with the application of an ac gate voltage to the dot energy level as well as the temperature gradient between the contacts.

We can represent the instantaneous behaviour of the dot energy level as

$$\epsilon_{dot}(t) = -5\Gamma - A\cos(\Omega t). \quad (12)$$

where A is the driving amplitude and Ω is the driving frequency. This kind of perturbation causes a continuous implicit change in Kondo temperature T_K because the dot energy level affects T_K according to Eq. (6). This results in a constant change in the shape of the Kondo resonance. The situation under consideration is depicted schematically in Fig. 15.

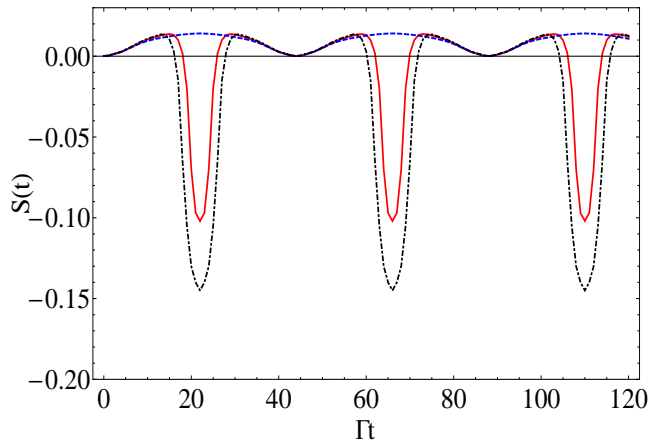


FIG. 16: This figure shows the instantaneous thermopower $S(t)$ immediately after the gate voltage has been turned on for driving amplitudes of 2.0Γ (blue dashed), 2.5Γ (red solid) and 3.0Γ (black dot dashed) at $T=0.003\Gamma$ and $\Omega=0.14\Gamma$ in linear response.

Fig. 16 shows instantaneous thermopower for three different driving amplitudes A at fixed driving frequency and ambient temperature after the gate voltage is applied. Thermopower slowly starts to increase as the dot level approaches the Fermi level for all driving amplitudes. For the smallest driving amplitude, it reaches a peak value at its closest point to the Fermi level and then gradually decreases again to zero as the dot level is moved away from the Fermi level. This monotonic behaviour is altered as the driving amplitude is ramped up. When $A = 2.5\Gamma$, the instantaneous thermopower initially grows in the positive region similar to the previous case. This similarity ends as the dot level comes close to the Fermi level because the instantaneous thermopower abruptly starts to decrease and dives into negative region before bouncing back. In ever higher driving amplitudes, instantaneous thermopower starts its descent earlier. Furthermore, it goes deeper into negative territory before rebounding with retreating dot level. These fluctuations are repeated in every period of dot level oscillation.

In Fig. 17, we calculate the instantaneous thermopower with a smaller driving frequency than the one in Fig. 16. All other parameters are unchanged. This choice naturally leads to longer oscillation periods for all driving amplitudes. Beyond this triviality, we see that the fairly smooth oscillation pattern for the smallest driving amplitude is still intact. The fluctuations of the other two larger driving amplitude cases also look similar to the larger driving frequency case but they both dive much deeper into negative territory when the dot level is in the vicinity of the Fermi level.

In order to determine whether these particular outcomes are valid for other driving frequencies and amplitudes, we performed an analysis by averaging the value of the instantaneous thermopower over a full period for two different ambient temperatures at several different driv-

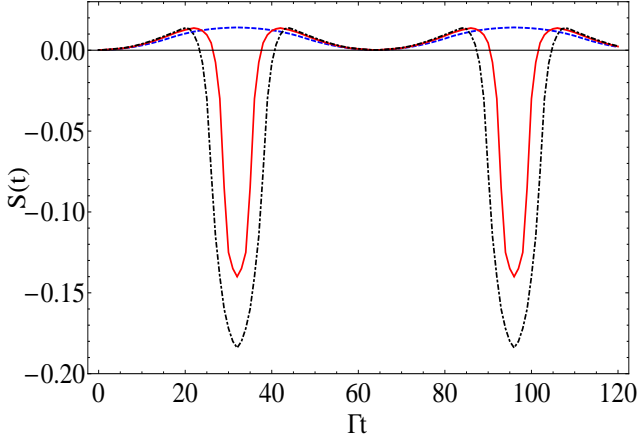


FIG. 17: This figure shows the instantaneous thermopower $S(t)$ immediately after the gate voltage has been turned on for driving amplitudes of 2.0Γ (blue dashed), 2.5Γ (red solid) and 3.0Γ (black dot dashed) at $T=0.003\Gamma$ and $\Omega=0.10\Gamma$ in linear response.

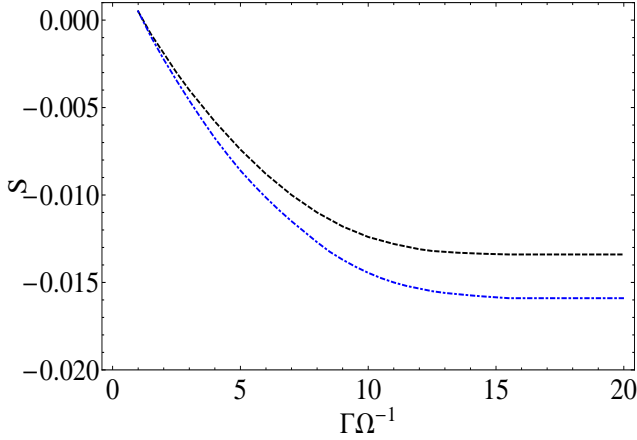


FIG. 18: This figure shows the value of the thermopower averaged over a period as a function of inverse driving frequency at $T=0.003\Gamma$ (black dashed) and $T=0.002\Gamma$ (blue dot dashed) for driving amplitude of 2.5Γ .

ing frequencies. We will omit the smallest driving amplitude because time averaged thermopower was insensitive to the changes in temperature for it. The time averaged value of the instantaneous thermopower is shown in Fig. 18 as a function of inverse driving frequency for two different ambient temperatures with $A = 2.5\Gamma$. First of all, altering the ambient temperature results in a change in absolute value of the time averaged thermopower at all driving frequencies. Furthermore, absolute value of the time averaged thermopower starts to increase at both temperatures with decreasing driving frequency but it saturates below a certain driving frequency.

We then extended this analysis to the largest driving amplitude of 3.0Γ keeping all other parameters constant. The result is seen in Fig. 19 which confirms the previous conclusions about the sensitivity of the time averaged

thermopower to ambient temperature and its saturation below a certain driving frequency. However, absolute values of the time averaged thermopower at both ambient temperatures and all driving frequencies are greater than the case in Fig. 18 with 2.5Γ .

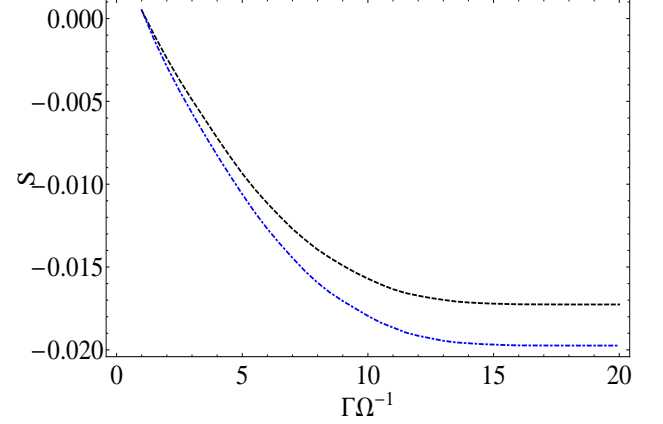


FIG. 19: This figure shows the value of the thermopower averaged over a period as a function of inverse driving frequency at $T=0.003\Gamma$ (black dashed) and $T=0.002\Gamma$ (blue dot dashed) for driving amplitude of 3.0Γ .

The dot level cannot sufficiently come close to the Fermi level to acquire the Kondo resonance when the driving amplitude is 2.0Γ . This means that $T \gg T_K$ throughout this oscillation and consequently the thermopower manages to stay in positive territory. It is zero at the furthest position of the dot level from the Fermi level since the density of states vanishes around the Fermi level. It then slowly starts to increase as the dot level approaches the Fermi level because the tail of the Breit-Wigner resonance starts to touch the Fermi level giving rise to a negative slope. Thermopower hits a peak positive value when the dot level is closest to the Fermi level. Thermopower starts to decrease as the dot level starts to move away. The lack of sensitivity to ambient temperature for this driving amplitude is related to the absence of Kondo resonance everywhere in this motion.

Boosting the driving amplitude to 2.5Γ makes the oscillation of the dot energy level cover a larger energy range. The instantaneous thermopower initially follows the curve obtained for 2.0Γ . Nevertheless, it begins to deviate considerably when the dot level approaches the Fermi level due to the emergence of the Kondo resonance. This implies a shift in slope of the density of states of the dot accompanied by a change in sign of the thermopower. When the dot level is at its closest point to the Fermi level, thermopower reaches a bottom since the Kondo resonance is in its most developed shape at that point. When the dot level starts to move away from the Fermi level, the Kondo resonance disappears gradually, hence the thermopower climbs out of the bottom becoming positive after a while. The instantaneous thermopower curve is quite similar for the largest driving amplitude of 3.0Γ except two differences. The instant-

neous thermopower dips lower and earlier into negative region simply because the dot energy level is closer to the Fermi level at any given time.

The evolution of the Kondo resonance is also the underlying factor behind the saturation of the time averaged thermopower at low driving frequencies. As the driving frequency is lowered, The dot energy level finds the chance to spend more time near the Fermi level with decreasing driving frequency. Since the formation of the Kondo resonance requires long time⁶, this sets aside more time for the Kondo resonance to develop. As a result, time averaged thermopower grows in negative territory until it saturates below a certain driving frequency. Saturation stems from the allocation of sufficient time for the full development of the Kondo resonance.

Finally, we want to elaborate on the dependence of the time averaged thermopower on temperature. Both Fig. 18 and Fig. 19 reveal that the difference between the time averaged values at the same driving frequency increases with decreasing driving frequency before saturating below a certain frequency. This underpins the significance of the development of the Kondo resonance. The lack of sensitivity of time averaged thermopower to ambient temperature at elevated driving frequencies stems from the insufficient time allocated to the dot level to spend around the Fermi level. This prevents the development of the Kondo resonance to its full extent. As the driving frequency is reduced, the difference becomes more discernible with decreasing driving frequency until it saturates at some point because the Kondo resonance is fully developed below that frequency.

V. CONCLUSION

In this chapter, we summarized the recent developments in time dependent electron transport through a

strongly correlated single electron transistor. In section II, we demonstrated that the discontinuities in the density of states of the electrodes can induce oscillations in the transient current whose frequency is proportional to the energetic separation between the Fermi level and the position of the discontinuity. Strong electron-phonon coupling on the dot has been shown in section III to give rise to oscillations in transient current whose frequency is equal to the phonon frequency. Finally, we investigated the evolution of Seebeck coefficient or thermopower in section IV. For the case where the dot level is abruptly changed, we determined that the decay time of thermopower to its steady state value saturates below the Kondo temperature. On the other hand, the instantaneous thermopower dips into negative region if the driving amplitude is ramped up such that the Kondo resonance finds time to develop.

We think that our findings are crucial to design the switching behaviour of next generation transistors that are expected to replace the current MOSFET's in near future. In that sense, our results have widespread ramifications along several disciplines such as physics, material science and electrical engineering. We also believe that state of the art ultrafast pump-probe techniques^{39,40} enable the experimental realization of our results. Consequently, our results in this chapter should pave the way for new experiments in this field.

VI. ACKNOWLEDGMENTS

Both authors thank Tübitak for generous financial support via grant 111T303. AG is indebted to Dr. Udo Schwingenschlogl and Dr. Xuhui Wang for several fruitful discussions and thanks Dr. Peter Nordlander for introducing this subject to him many years ago.

-
- ¹ Likharev K K 2003 in J Greer, A Korkin and J Labanowski, eds, *Nano and Giga challenges in microelectronics* (Dordrecht: Elsevier) pp 27–68
 - ² Elzerman J M, Hanson R, van Beveren L H W, Witkamp B, Vandersypen L M K and Kouwenhoven L P 2004 *Nature(London)* **430** 431–434
 - ³ Fève G, Mahe A, Berroir J M, Kontos T, Placais B, Glattli D C, Cavanna A, Etienne B and Jin Y 2007 *Science* **316** 1169
 - ⁴ Plihal M, Langreth D C and Nordlander P 2005 *Phys. Rev. B* **71** 165321
 - ⁵ Izmaylov A F, Goker A, Friedman B A and Nordlander P 2006 *J. Phys.: Condens. Matter* **18** 8995–9006
 - ⁶ Nordlander P, Pustilnik M, Meir Y, Wingreen N S and Langreth D C 1999 *Phys. Rev. Lett.* **83** 808–811
 - ⁷ Plihal M, Langreth D C and Nordlander P 2000 *Phys. Rev. B* **61** R13341–13344
 - ⁸ Merino J and Marston J B 2004 *Phys. Rev. B* **69** 115304
 - ⁹ Goker A, Friedman B A and Nordlander P 2007 *J. Phys.: Condens. Matter* **19** 376206
 - ¹⁰ Goker A, Zhu Z Y, Manchon A and Schwingenschlogl U 2010 *Phys. Rev. B* **82** 161304(R)
 - ¹¹ Goker A, Zhu Z Y, Manchon A and Schwingenschlogl U 2011 *Chem. Phys. Lett.* **509** 48
 - ¹² Goker A 2011 *J. Phys.:Condens. Matter* **23** 125302
 - ¹³ Reddy P, Jang S Y, Segalman R A and Majumdar A 2007 *Science* **315** 1568
 - ¹⁴ Baheti K, Malen J A, Doak P, Reddy P, Jang S Y, Tilley T D, Majumdar A and Segalman R A 2008 *Nano Lett.* **8** 715
 - ¹⁵ Malen J A, Doak P, Baheti K, Tilley T D, Majumdar A and Segalman R A 2009 *Nano Lett.* **9** 3406
 - ¹⁶ Tan A, Sadat S and Reddy P 2010 *Appl. Phys. Lett.* **96** 13110
 - ¹⁷ Dong B and Lei X L 2002 *J. Phys.:Condens. Matter* **14** 11747
 - ¹⁸ Costi T A and Zlatić V 2010 *Phys. Rev. B* **81** 235127
 - ¹⁹ Goker A and Uyanik B 2012 *Phys. Lett. A* **376** 2735

- ²⁰ Al-Hassanieh K A, Busser C A, Martins G B and Dagotto E 2005 *Phys. Rev. Lett.* **95** 256807
- ²¹ Kiselev M N, Kikoin K, Shekhter R I and Vinokur V M 2006 *Phys. Rev. B* **74** 233403
- ²² Scheible D V, Weiss C, Kotthaus J P and Blick R H 2004 *Phys. Rev. Lett.* **93** 186801
- ²³ Parks J J, Champagne A R, Hutchison G R, Flores-Torres S, Abruna H D and Ralph D C 2007 *Phys. Rev. Lett.* **99** 026601
- ²⁴ Goker A 2008 *Solid State Comm.* **148** 230
- ²⁵ Goker A and Gedik E 2012 submitted
- ²⁶ Shao H X, Langreth D C and Nordlander P 1994 *Phys. Rev. B* **49** 13929–13947
- ²⁷ Blaha P, Schwarz K, Madsen G K H, Kvasnicka D and Luitz L 2001 *WIEN2K, an augmented plane wave+local orbitals program for calculating crystal properties* (Wien: Techn. Universität)
- ²⁸ Perdew J P, Burke K and Ernzerhof M 1996 *Phys. Rev. Lett.* **77** 3865
- ²⁹ Jauho A P, Wingreen N S and Meir Y 1994 *Phys. Rev. B* **50** 5528
- ³⁰ Galperin M, Nitzan A and Ratner M A 2007 *Phys. Rev. B* **76** 035301
- ³¹ Muhlbacher L and Rabani E 2008 *Phys. Rev. Lett.* **100** 176403
- ³² Chen Z Z, Lu R and Zhu B F 2005 *Phys. Rev. B* **71** 165324
- ³³ Galperin M, Nitzan A and Ratner M A 2006 *Phys. Rev. B* **73** 045314
- ³⁴ Wang R Q, Zhou Y Q, Wang B and Xing D Y 2007 *Phys. Rev. B* **75** 045318
- ³⁵ Paaske J and Flensberg K 2005 *Phys. Rev. Lett.* **94** 176801
- ³⁶ Yang K H, Wu Y P and Zhao Y L 2010 *Europhys. Lett.* **89** 37008
- ³⁷ Costi T A, Hewson A C and Zlatić V 1994 *J. Phys.:Condens. Matter* **6** 2519
- ³⁸ Chi F and Dubi Y 2012 *J. Phys.:Condens. Matter* **24** 145301
- ³⁹ Terada Y, Yoshida S, Takeuchi O and Shigekawa H 2010 *J. Phys.: Condens. Matter* **22** 264008
- ⁴⁰ Terada Y, Yoshida S, Takeuchi O and Shigekawa H 2010 *Nat. Photon.* **4** 869